

RESEARCH ARTICLE

Open Access



Crustal deformation detection capability of the GNSS-A seafloor geodetic observation array (SGO-A), provided by Japan Coast Guard

Yusuke Yokota^{1*} , Tadashi Ishikawa², Shun-ichi Watanabe² and Yuto Nakamura²

Abstract

The GNSS-A technique is an observation method that can detect seafloor crustal deformations with centimeter-level positioning accuracy. The GNSS-A seafloor geodetic observation array operated by the Japan Coast Guard (SGO-A) has been constructed near the Japanese Islands along the Nankai Trough and the Japan Trench. This observation array has detected several earthquakes' displacements and episodic slow crustal deformation. To compare the detection results of SGO-A with other observation networks and expand the SGO-A coverage area, it is necessary to correctly understand its detection capability. In this paper, numerical simulations and statistical verifications were used to assess the capabilities of the present GNSS-A system using a manned vessel (observation frequency: 4–6 times/year, positioning accuracy: standard deviation = 1.5 cm) to detect (1) secular deformation only, (2) a transient slip event only and (3) secular deformation and a transient event together. We verified these results with appropriate thresholds and found the following features: When it is known that there is no transient event, the 95% confidence level (CL) for the estimation of secular crustal deformation rate with 4-year observation is about 0.5–0.8 cm/year; when the deformation rate is known, a signal of about 3.0 cm can be detected by observations of about 4 times before and after the transient event. When the deformation rate and the transient event are detected together, to keep the false positive low (about 0.05), the false negative becomes high (about 0.7–0.2 for detecting a signal of 4.5–6.0 cm). The determined rate and event variations are approximately 1.8 cm/year (95%CL) and 1.5 cm (standard deviation), respectively. We also examined the detection capability for higher observation frequency and positioning accuracy, to examine how the detection capability improves by technological advancements in the future. Additionally, we calculated the spatial range of event detectability using the determined values of detection sensitivity. Obtained results show that each seafloor site can detect a slip event of < 1.0 m scale within about 30 km radius, and approximately one-third of the subseafloor slip event over 100 km from land along the Nankai Trough can only be detected by SGO-A.

Keywords: GNSS-A, SGO-A, Seafloor geodetic observation, Earthquake detection limit, SSE detection limit

1 Introduction

A subduction zone where a tectonic plate subducts beneath another plate frequently causes megathrust earthquakes. To prevent associated disasters, it is important to elucidate the physical mechanism involved in

such earthquakes. Accurate monitoring of crustal activities related to the earthquake cycle, i.e., inter-, co- and post-seismic processes, plays an essential role for this purpose. Because the cycle contains many types of geophysical phenomena with different time scales, many types of geodetic and seismological observations are conducted to monitor them (Table 1). These observations contribute to the understanding of surface oscillations and crustal movements caused by subsurface geophysical phenomena.

*Correspondence: yyokota@iis.u-tokyo.ac.jp

¹ Institute of Industrial Science, University of Tokyo, 4-6-1 Komaba, Meguro-ku, Tokyo 153-8505, Japan

Full list of author information is available at the end of the article

Table 1 Signals related to the earthquake cycle.

Seismic cycle	Geophysical phenomena	Time scale	Observation type	Observation instruments	Typical signal pattern	Subsection in this paper
Inter-seismic	Strain accumulation due to plate coupling or block motions	10 Years	Geodetic	GNSS / GNSS-A	Steady trend	2.1
	long term	1 Year			Transient change	2.2, 2.3
	Slow Slip Event (SSE)	100 Days		Strainmeter Tiltmeter		
	short term	1 Day				
Co-seismic	Very Low Frequency Earthquake (VLFE) Tremor	10 Seconds	Seismic	Seismometer	Oscillation	
	Earthquake	1 Second				
	(Permanent deformation)	10 Seconds	Geodetic	GNSS / GNSS-A	Non-continuous step	2.2
Post-seismic	Stress relaxation	1 Year 10 Years			Non-linear change	(2.1)

Space geodetic observation techniques such as the Global Navigation Satellite System (GNSS) mainly contribute to the monitoring of long-term phenomena such as inter- and post-seismic processes and permanent displacement associated with co-seismic process. However, because most of the subducting plate boundaries, which are the focal regions of megathrust earthquakes, are located underneath the seafloor far away from the coast, it is difficult to monitor these phenomena accurately by terrestrial GNSS (e.g., Yoshioka and Matsuoka 2013; Schmalzle et al. 2014; Williamson and Newman 2018).

GNSS-A (Global Navigation Satellite System–acoustic ranging combination technique) is a new seafloor geodetic observation technique capable of measuring such subseafloor boundary processes by combining GNSS and underwater acoustic ranging (Spiess 1985; Asada and Yabuki 2001; Fujita et al. 2006). Along the Japan Trench and the Nankai Trough, the GNSS-A seafloor geodetic observation array (SGO-A) has been deployed by the Japan Coast Guard. SGO-A succeeded in detecting various geodetic phenomena on the seafloor, e.g., interplate coupling condition estimated from long-term crustal velocity (Yokota et al. 2016), transient motions due to slow slip events (SSEs) (Yokota and Ishikawa 2020), co-seismic slips (Sato et al. 2011) and time-dependent post-seismic deformation (Watanabe et al. 2014, 2021).

However, compared to land-based GNSS, seafloor GNSS-A presently has limited spatiotemporal resolution and positioning accuracy to detect geodetic phenomena. GNSS-A requires a sea surface platform to combine the GNSS positioning and acoustic ranging. While GNSS has achieved continuous observation networks, GNSS-A is limited to discontinuous

campaign observation, because the present platform is mainly a manned vessel. The annual observation frequency of GNSS-A operated by Japan Coast Guard is at least about 4 times per site (Ishikawa et al. 2020). In the future, the observation frequency is expected to be upgraded by buoys and self-propelled sea surface platforms (e.g., Tadokoro et al. 2020; Foster et al. 2020; Iinuma et al. 2021).

In the best cases, the standard deviation (σ) of the GNSS-A data is about 1.5 cm for the horizontal component, using the present analysis method (Watanabe et al. 2020). Empirically, the positioning uncertainty can be considered as Gaussian noise (Yokota et al. 2018). The main sources of noise are spatiotemporally multi-scale ocean disturbances such as short-term perturbations, diurnal fluctuations, ocean currents and others. Although the researchers try to reduce the effect by sophisticating their models (e.g., Yokota et al. 2019, 2020; Yokota and Ishikawa 2019; Kinugasa et al. 2020; Watanabe et al. 2020), it is still difficult to completely model them. Incompleteness of the ocean model causes systematic bias in positioning, i.e., outliers in time series unexpected from Gaussian noise. In addition, random walk noise of GNSS positioning, or unexpected equipment error, e.g., misalignment of equipment mounting position in sea surface unit, may cause systematic bias in positioning. These systematic errors, which cannot be controlled by the present analysis and observation systems, are not treated in this paper.

This positioning accuracy is much worse than the daily coordinate data ($\sigma \leq 0.5$ cm) of terrestrial GNSS observation networks such as the GEONET (Nakagawa

et al. 2009). Moreover, the distance between SGO-A sites is about 100 km, while that of the GEONET is about 30 km, and the low spatial density of observation sites caused lower-spatial-resolution offshore than for the onshore area.

Due to these limitations, it is necessary to collect enough data through long-term observations to detect geodetic phenomena accurately by GNSS-A. In addition, the magnitude of the phenomena must be large enough to be detected. In this paper, we examined the detection capability of the geodetic phenomena shown in Table 1 from temporally sparse geodetic time series data using statistical test and numerical experiments. Because the detection conditions differ depending on the known information and the target event, tests were conducted under three types of conditions. Additionally, we examined the ability to detect interplate boundary slip in the present SGO-A along the Nankai Trough and the Japan Trench.

2 Detection capability tests: methods

Seismic cycle geophysical phenomena observed geodetically can be broadly divided into four types, as shown in Table 1. Steady secular crustal deformation due to plate coupling or rigid block motions in the absence of transient events is simply detected as linear steady trends (gray column in Table 1). The trend is estimated by regression analysis (Fig. 1a). The effect of the amount and duration of the data on the estimation of the trend is discussed in subsections ‘Trend estimation.’ Regular earthquakes and cumulative displacement of SSEs are detected as non-continuous step signals (yellow column in Table 1). The step is estimated by taking the difference between the average positions before and after the transient event (Fig. 1b). The effect of the number of observations on the statistical test of the significance of the step is discussed in subsections ‘Step detection without trend.’ In the real systems, the trend and the step are often estimated simultaneously (blue column in Table 1). Thus, in subsections ‘Step detection with trend,’ we discuss the methods for estimating these two values simultaneously and their uncertainties (Fig. 1c). Post-seismic deformation is detected as non-linear change that decreases with time (brown column in Table 1). To estimate the change, various models have been considered such as logarithmic or exponential. In this paper, although we do not consider nonlinear change of time series due to the complexity of models, we discuss it supplementarily in subsections ‘Trend estimation.’

We examined the ability of temporally sparse geodetic data to detect these phenomena using virtual datasets. In the following verifications, we assumed that the time series data have a Gaussian noise with standard deviation

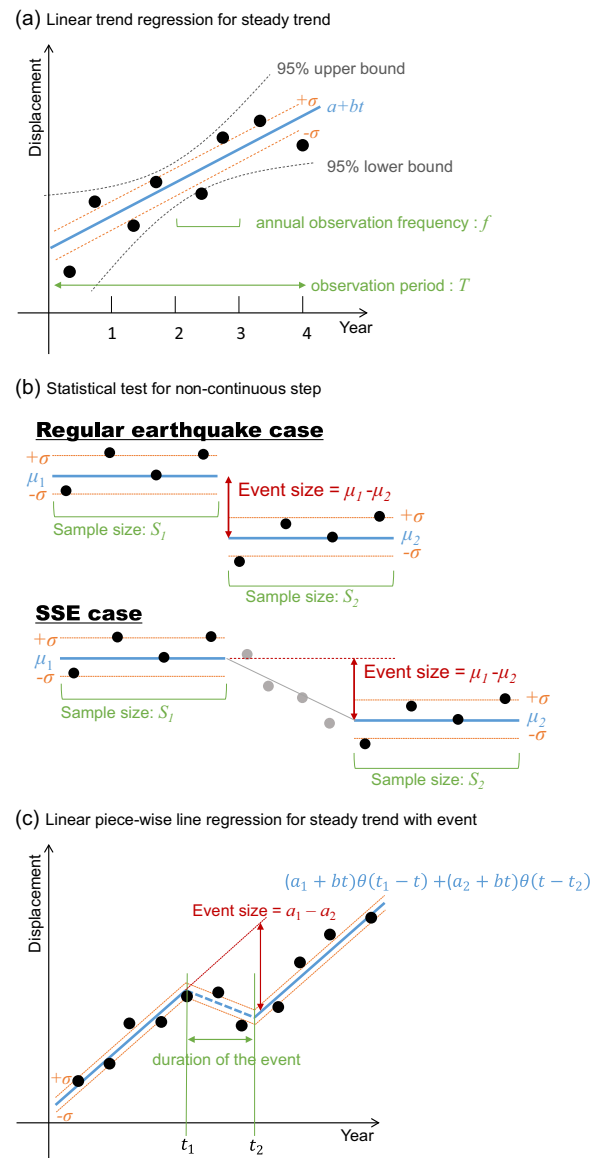


Fig. 1 **a** An example of virtual time series used in Sect. 2.1 in the case of observation frequency (f) = 2 times/year. Blue, orange and gray lines indicate a fitting line, $\pm 1\sigma$ ranges and the 95% confidence levels (CL) for the linear fitting, respectively. Green arrow indicates an observation period (T). **b** An example of virtual time series used in Sect. 2.2 in a regular earthquake case (upper) and an SSE case (bottom). Sample sizes S_1 and S_2 are the numbers of the data before and after the event, respectively. An event size is depicted by a red arrow. **c** An example of virtual time series used in Sect. 2.3. In this virtual data, the standard deviation σ is given to the functions represented by Eqs. (3) and (4)

of σ . In the latter half of subsections ‘Trend estimation’ and all of subsections ‘Step detection with trend,’ we verified by numerical simulations using pseudodata.

2.1 Trend estimation

First, we describe methods to assess the uncertainty in quantifying a secular deformation that results from plate motion or rigid block motion, which is observed as a linear trend (Fig. 1a). To detect the heterogeneity of plate coupling in the source region of the megathrust earthquake, it is necessary to estimate the velocity with an accuracy of less than 1 cm/year. Here, we assessed how much data are needed for this purpose.

We considered time series (annual observation frequency= f) having the standard deviation σ along a linear function for an observation period (T) (as shown in Fig. 1a). The trend was estimated by linear regression with a linear function, $a + bt$ (a and b are model parameters unknown to be estimated). The unbiased variance of the trend b is represented as

$$\text{Var}(b) = \frac{\sigma^2}{\sum_i (t_i - \bar{t})^2}, \quad (1)$$

where t_i is the time of i th data, σ is the standard deviation of data and \bar{t} is the average of t_i . At this time, since the result depends on σ , a result can be applied to any σ data by normalizing with σ .

To verify the heterogeneity detection of the crustal velocity field, the significance test of the differences of the trend among adjacent sites is necessary. This test is also effective to detect the temporal variation between two periods in the case of a nonlinear trend such as post-seismic deformation. For this test, we numerically generated pseudodata as shown in Fig. 1a along a linear function. We conducted a statistical hypothesis test to examine whether the null hypothesis that the trends of two time series are the same can be rejected at a significance level of 0.05. Here, we tested by 1000 numerical experiments on two pseudodata with the same period and observation frequency.

2.2 Step detection without trend

In this subsection, we describe methods to assess the uncertainty in quantifying a transient deformation that results from earthquake or SSE, which is observed as a steplike signal (Fig. 1b). When a seismic event occurs, a steplike signal appears in the time series. The step is detected from the difference between the average positions before and after the transient event. In this subsection, we examined the effect of the number of the data on the statistical test of the significance of the step. For simplicity, we assumed that there is no trend in the time series of our statistical tests. This means that either the trend has been removed by trend estimation, or the period of the data is short enough to neglect the trend. Simultaneous estimation of both trend and step is discussed in the next subsection.

We considered the case of detecting a signal in a time series as shown in Fig. 1b and conducted a statistical test for the difference between the mean value before and after the transient event. The significance of the event is judged based on whether the null hypothesis that the mean value before and after the transient event is equal is rejected or not. There are two types of errors in the statistical test. A type I error (false positive) α is the rejection of a true null hypothesis and a type II error (false negative) β is the non-rejection of a false null hypothesis. To detect an event accurately, these two types of errors need to be small. The condition is determined by the number of the data (sample size) and the magnitude of the event (effect size).

The statistical power γ (probability of correctly detecting a significant difference Δ (effect size)) is defined as

$$\gamma \equiv 1 - \beta = P\left(Z_1 \leq Z(\alpha/2) + \Delta\sqrt{n}\right) + P\left(Z_1 \geq Z(\alpha/2) - \Delta\sqrt{n}\right). \quad (2)$$

Parameters in the equations are defined as follows: P : one-sided probability of Gaussian distribution, Z_i : test statistic, Z : value in Gaussian distribution, n : sample size, Δ : effect size (difference between the mean values of the two samples normalized by the standard deviation.), α : two-sided confidence level (false positive rate), Δ for n is discussed at a certain threshold value for γ . Here, Δ was determined from Eq. (2) when $\gamma=0.8$, which is generally used. We determined n (the number of observations before and after the transient event) as the minimum sample size for Δ .

To verify the accuracy of the step detection, the uncertainty (standard deviation: σ_s) of the detected step was also estimated by Eq. (2) for the case of having a certain step at the center of the observation period. The results are evaluated by standardizing with σ .

2.3 Step detection with trend

In the actual geodetic time series, it is necessary to detect the transient event from a short time series, in which the trend and the timing of the event are unknown. We here describe a method to assess the uncertainty in quantifying a trend and a transient deformation that results from earthquake or SSE during plate motion or rigid block motion (Fig. 1c). If the trend is assumed to be unchanged before and after the transient event, the time series is represented as a piecewise line (Fig. 1c) as follows,

$$f(t) = (a_1 + bt)\theta(t_1 - t) + (a_2 + bt)\theta(t - t_2), \quad (3)$$

$$\theta(t) = \begin{cases} 1 & (t > 0) \\ 0 & (t < 0) \end{cases}, \quad (4)$$

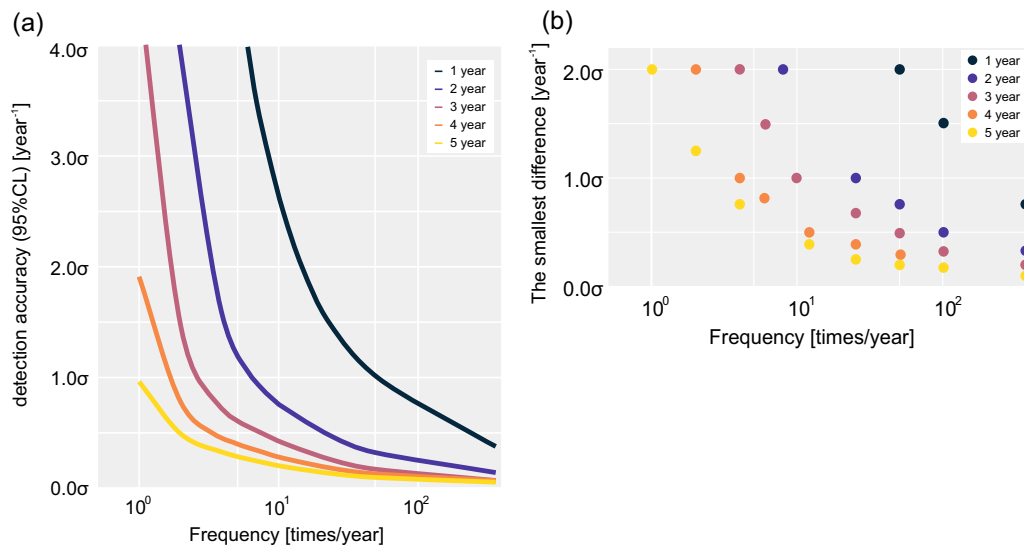


Fig. 2 **a** 95%CL of detected trend with respect to the observation frequency, with each color corresponding to an observation period between 1 and 5 year. **b** Smallest difference in the trends that can reject the null hypothesis that the trends are same, at a significance level of 0.05

where t_1 and t_2 are the beginning and the ending times of the transient event, respectively. Because the estimation of t_1 and t_2 is a nonlinear regression problem, we used the numerical estimation using grid search which is similar to the method proposed in Yokota and Ishikawa (2020). Once t_1 and t_2 are fixed, fitting a piecewise line is a linear regression problem. We searched the best result which minimizes the c-AIC (Akaike 1974; Sugiura 1978), by varying t_1 every 0.1 year. The duration of the transient event ($t_2 - t_1$) is fixed to 1 year; the uncertainty of the estimation of duration is discussed later. The c-AIC is defined as follows:

$$\text{c-AIC} = m \ln(2\pi) + m \ln\left(\frac{RSS}{m}\right) + \frac{2mk}{m-k-1}, \quad (5)$$

where m , k and RSS are the number of total data, number of model parameters and the residual sum of squares, respectively. In addition, we calculated the c-AIC when fitting a straight line, which assume no transient event in the time series. If the c-AIC when fitting a piecewise line is smaller than that of a straight line, the transient event has been detected statistically. Here, we used $\Delta\text{c-AIC}$ ((c-AIC when fitting a piecewise line)–(c-AIC when fitting a straight line)).

To verify the detection capability of the trend and the step, we examined the difference between the model estimated from pseudodata and the original model. Based on the result of Sects. 2.1 and 3.1, we numerically generated 6-year time series pseudodata for stable estimation of the trend, and the 1-year transient event was set in the center of the time series as shown in Fig. 1c. The duration of the

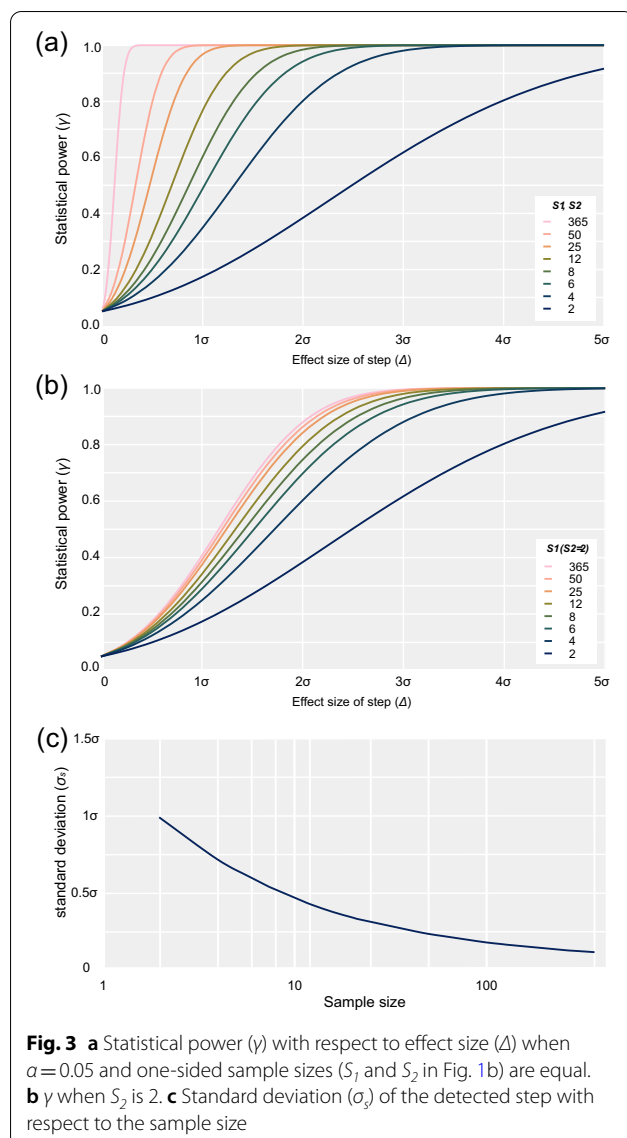
transient event was fixed to 1 year also in the estimation. Pseudodata were created adding a Gaussian noise (standard deviation = σ) to the original model described above created according to Eqs. (3) and (4). We used pseudodata with various event size (D : deformation size) and the observation frequency (f) and examined in each case with 1000 trials. Here, we tried D from 0 to 8σ and f from 1 to 365 times/year. The verification results are evaluated by standardizing with σ .

3 Detection capability tests: results

3.1 Trend estimation

Figure 2a shows the 95% confidence level (CL) of the trend normalized by σ with respect to f calculated by Eq. (1). 95%CL is calculated using Student's t-distribution function (Student 1908). Each color of the series represents the cases of T of 1–5 years. In the case of $f \sim 4$ –6 times/year, which is equivalent to the present GNSS-A observation using a manned vessel (vessel-GNSS-A), at least 4 years of observation is required to achieve an accuracy of about 0.5σ /year. For example, with the present vessel-GNSS-A data of $\sigma = 1.5$ cm, an accuracy of approximately 0.5–0.8 cm/year is achieved by observing for 4 years. If daily observation ($f = 365$ times/year) is realized, an accuracy of less than 1.0 cm/year will be achieved by less than 1 year of observation.

The results of the significant test using numerical pseudodata show the smallest difference of trends for which the null hypothesis is rejected at the 0.05 level (Fig. 2b). Detectable differences are about twice as large as the



95%CL trend sensitivity for a given observation frequency and duration. The present vessel-GNSS-A can detect a difference of approximately 1.0–1.5 cm/year by observing for 4 years.

3.2 Step detection without trend

Figure 3a shows γ with respect to Δ for $\alpha = 0.05$. The sample sizes (n) before and after the transient event, S_1 and S_2 , respectively, are set to be equal. The statistical power increases with increasing sample size and effect size. When the threshold of γ is set to 0.8, sample size of 12 and 4 are required to detect transient events with size of 1σ and 2σ , respectively. Figure 3c shows σ_s of the detected step size with respect to the sample size obtained by the law of propagation of errors. σ_s decreases

according to $1/\sqrt{n}$. When observing one year before and after the transient event, the sample size equals the observation frequency.

When an earthquake or SSE occurs, it is necessary to detect permanent crustal deformations urgently, for the rapid evaluation of the event. Because there is a large amount of uncertainty in one-time observation, we here consider two-time observation after the event. Figure 3b shows γ when the sample size after the event (S_2 in Fig. 1b) is set to 2. When the threshold of γ is set to 0.8, S_1 (in Fig. 1b) are 12 and 4 to detect events of 2σ and 2.7σ , respectively.

3.3 Step detection with trend

Here, we first examined the detection probability of the transient event. Figure 4a shows the rate of false positive of our method, i.e., the probability that the piecewise line is incorrectly determined to be more significant than the straight line despite the absence of an event ($D=0$), when applying thresholds of 0, 5 and 10 for the $-\Delta c-AIC$. If the threshold is set to 0, the false detection rate becomes larger than 0.6–0.7, suggesting that this threshold cannot be used practically for detection of a step in a trend. The false detection rate can be improved by increasing the threshold; in the case where the threshold is set to 10, the false detection rate is about less than 0.05, which can be used practically.

Figure 4b–d show the probability of false negative of our method, i.e., when the piecewise line is incorrectly determined to be less significant than the straight line, despite the existence of an event, when applying thresholds of 0, 5 and 10 for the $-\Delta c-AIC$. It decreases by increasing annual observation frequency and event size. Contrary to the case of the false positive, the false negative rate increases by increasing the threshold of $-\Delta c-AIC$. For the actual geodetic time series, it is necessary to set appropriate thresholds according to the purpose, due to the trade-off relation between false positive and false negative. For example, accepting a high false negative rate will decrease the false positive rate due to the trade-off relation. However, a high false negative rate indicates that we are failing to detect many of the transient events that are actually occurring. On the other hand, an exceedingly high false positive rate indicates that we are detecting events that are not actually occurring, which might lead to false findings for research of the physical earthquake process. From the viewpoint of disaster prevention, it may be beneficial to issue an alarm, even if the predictions are likely to be wrong. Therefore, in some cases, it is necessary to accept false positive rate to some degree.

Increasing the observation frequency is effective in reducing the false negative rate while keeping the false positive rate low even for the detection of a small step signal. For example, according to Fig. 4d, if the observation

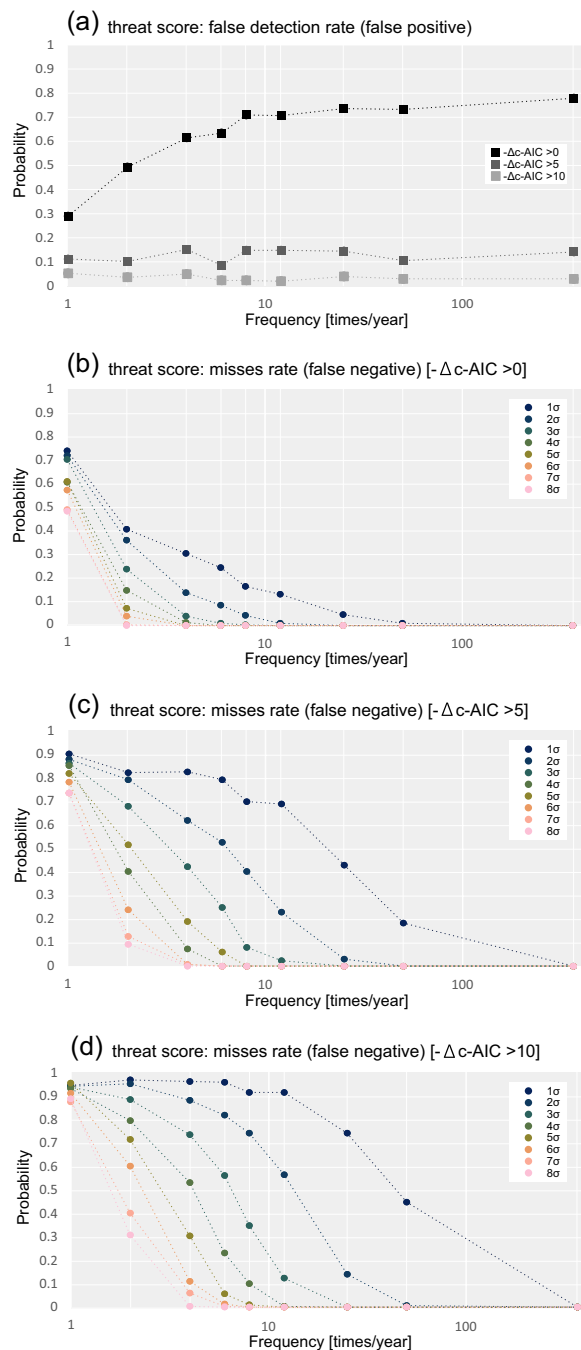


Fig. 4 Statistical summaries for the step signal detection probability in the trend and event detection. **a** False positive at each observation frequency, i.e., probability of the cases where an event is false detected in the no-event synthetic data. **b–d** False negative, i.e., probability of the cases where no or negative event is detected in the finite-event synthetic data; for the cases where the thresholds of $-\Delta c-AIC$ are 0, 5 and 10, respectively

frequency was improved from about every 2 months (6 times/year) to about every 2 weeks (25 times/year), the false negative rate of 0.8 for the 2σ step signal is improved to 0.15. In the case of GNSS-A using unmanned platforms, this is a realistic observation frequency.

Next, we examined the accuracy of trend and transient event determinations. Since the determination accuracy cannot be discussed for thresholds with high false positive rates, we evaluated the case of $-\Delta c-AIC > 10$ and $f = 2-365$ times/year. Figure 5 shows the difference (O–C) between the parameters of the estimated model and the original model. Comparing to the former subsections where the trend and step are estimated independently (Figs. 2 and 3), the accuracy of trend and step estimation becomes worse when these parameters are estimated simultaneously (Fig. 5a, b). Figure 5c shows the 90th percentile width, median and average of O–C of occurrence times. These results suggest that the occurrence time can be determined approximately ± 0.5 years with a 90% probability in cases where the annual observation frequency is larger than 4 times/year and the event size is larger than 3σ .

4 Discussions

4.1 Summary of detection capability

As concrete cases, we compared the cases of campaign vessel-GNSS-A and daily-GNSS (Table 2). The annual observation frequency (f) and standard deviation of horizontal positioning (σ) of the present GNSS-A are 4–6 times/year and 1.5 cm, respectively (Ishikawa et al. 2020). In the case of daily-GNSS ($f = 365$ times/year), σ is better than 0.5 cm (e.g., Nakagawa et al. 2009; Suito 2016). Since the above tests depend on σ itself, detection capability of daily-GNSS with different σ and f can be derived from these test results.

We first considered the trend detection capability when it is known that there is no step (Fig. 2). In the case of daily-GNSS, it is possible to detect less than 0.5 cm/year (95%CL) even with 1-year observation. On the other hand, vessel-GNSS-A needs longer observation period to detect the trend accurately. According to Fig. 2a, vessel-GNSS-A can achieve an accuracy of less than 1 cm/year (0.5–0.8 cm/year) with 4-year observation. Differences between the deformation rate of observation sites or different time periods can be detected with the accuracy of 1.0–1.5 cm/year with 4-year observation according to Fig. 2b.

In the future, it may be possible for an advanced self-propelled buoy to observe a seafloor site about once a week, even if the weather and the sea surface environment is taken into consideration. Considering the positioning accuracy of GNSS, future GNSS-A may be

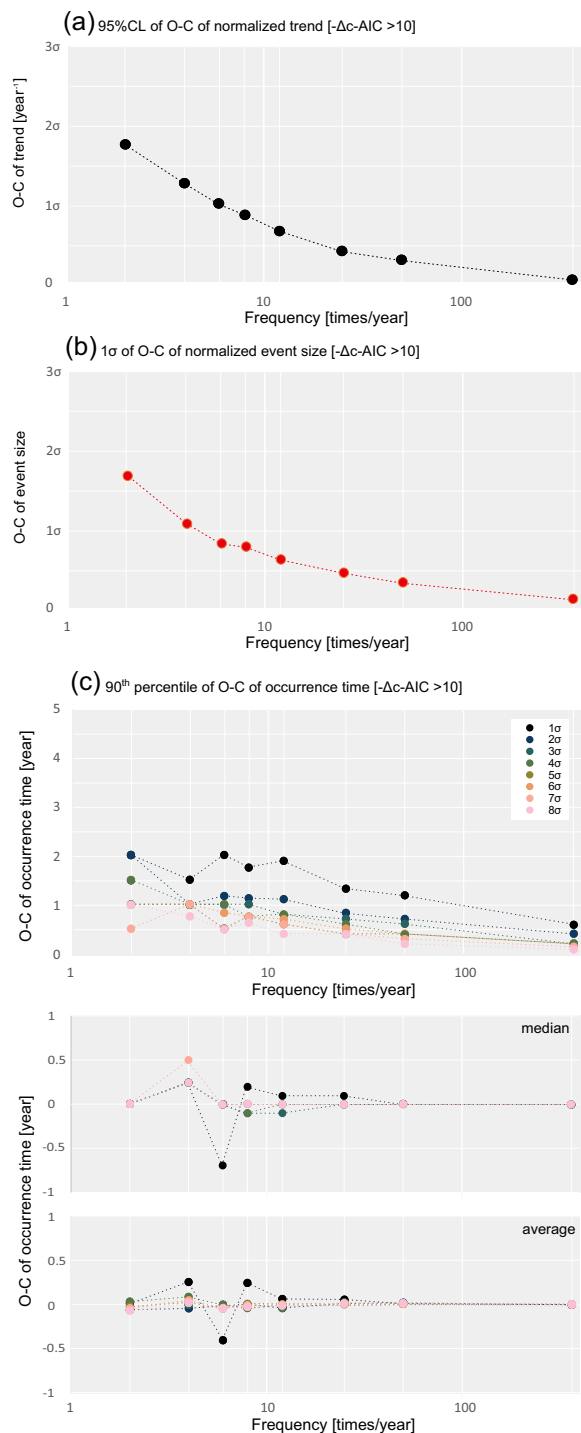


Fig. 5 Statistical summaries for the trend and event determination accuracy. **a** The 95%CL of O-C of normalized rate determined when the threshold of $-\Delta c\text{-AIC}$ is 10. **b** The standard deviation of O-C of normalized event size determined when the threshold of $-\Delta c\text{-AIC}$ is 10. **c** Occurrence time determination accuracy: the 90th percentile, median and average of O-C of occurrence time determined when the threshold of $-\Delta c\text{-AIC}$ is 10

improved up to about $\sigma = 1$ cm and $f = 50$ times/year. The improvement in f has a great effect especially when T is short. In $f = 50$ times/year, it is possible to detect the secular crustal deformation of $1.0\sigma/\text{year}$ and the difference of 2.0σ (1.0 cm/year and 2.0 cm in the future) even for 1-year observation.

The step detection capability when the trend can be ignored is shown in Fig. 3. In the case of daily-GNSS, it is possible to detect a step of less than 0.1 cm with the accuracy of $\sigma_s \sim 0.05$ cm by 1-year observation before and after the transient event according to Fig. 3a, c. On the other hand, in the case of vessel-GNSS-A, a step of 3.0 cm can be detected with the accuracy of $\sigma_s \sim 1.0$ cm by 1-year observation before and after the transient event.

According to Fig. 3b, daily-GNSS can detect a step of 1.0 cm even 2 days after the transient event. GNSS-A can detect a step of 4.0 cm by two observations after the transient event. Improving the observation frequency and positioning accuracy also has a positive effect on emergency detection. Especially when a step of 4.0 cm or more is predicted, two-time emergency observation should be performed.

We finally considered the detection capability and the accuracy when both trend and step should be considered (Figs. 4 and 5). In the case of daily-GNSS ($\sigma = 0.5$ cm, $f = 365$ times/year), when the threshold of $-\Delta c\text{-AIC}$ is set to 10, the false negative rate will be almost 0 according to Fig. 4a. The determination accuracy of trends and steps is 0.1 cm/year (95%CL), 0.1 cm or less (standard deviation), and the event occurrence time is also determined with the accuracy of ± 0.1 year (90th percentile) according to Fig. 5.

In the case of GNSS-A ($\sigma = 1.5$ cm, $f = 4\text{--}6$ times/year), when the threshold of $-\Delta c\text{-AIC}$ is set to 10, the false negative rate for the event size of 4.5–6.0 cm is 0.7–0.2 by 6-year observation, according to Fig. 4d. False negative rates for 4.5 cm events are high, but false negative rate drops sharply for 6.0 cm. The trend and step are determined with the accuracy of 1.8 cm/year (95%CL) and of 1.5 cm (standard deviation), respectively, according to Fig. 5a, b. For a step signal of 4.5–6.0 cm, the occurrence time of the transient event is determined with the accuracy of ± 0.5 years (90th percentile), according to Fig. 5c.

Even in this case, the false negative rate and the determination accuracy are improved depending on the positioning accuracy and observation frequency. For example, increasing the GNSS-A observation frequency to about 50 times/year (weekly) improves the false negative rate for 2σ (3.0 cm) events (Fig. 4d).

Although not covered in this study, the event duration is estimated from two unknown parameters, the occurrence time and the end time of the transient event. Therefore, the determination accuracy of the duration is always worse than that of the occurrence time.

Table 2 Summary of the signal detection and determination capabilities of vessel-GNSS-A and daily-GNSS in 2021




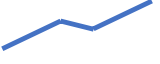
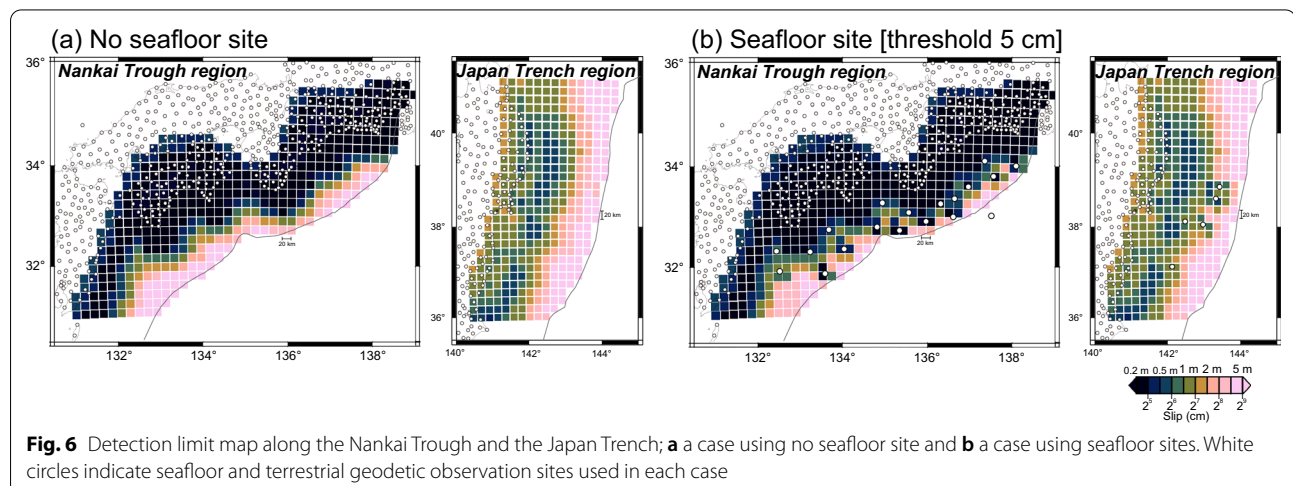
	Ability	GNSS-A	Daily-GNSS
	Observation frequency (f)	4–6 times/year	365 times/year
	Standard deviation (σ)	1.5 cm	0.5 cm
Case	Verification	GNSS-A	Daily-GNSS
Trend only 	95%CL of determined trend	6.0 cm/year (1-year obs.) 0.5–0.8 cm/year (4-year obs.)	0.2 cm/year (1-year obs.) 0.03 cm/year (4-year obs.)
	95%CL of detectable difference of trends	1.0–1.5 cm/year (4-year obs.)	0.35 cm/year (1-year obs.) 0.05 cm/year (4-year obs.)
Event only 	Effect size ($\gamma=0.8$ and $\alpha=0.05$)	3.0 cm (± 1 -year obs.)	0.1 cm (± 1 -year obs.)
	(For keeping a false positive below 0.05, threshold of $-\Delta c\text{-AIC}$ should be set about 10.)		
Trend and event (6-year obs.) 	False negative	0.7–0.2 (for a signal of 4.5–6.0 cm ($3\sigma\text{--}4\sigma$))	0 (even for a signal of 0.5 cm (1σ))
	95%CL of determined trend	1.8 cm/year (1.2 σ /year)	0.1 cm/year (0.18 σ /year)
	Standard deviation of determined event size	1.5 cm (1σ)	0.08 cm (0.15 σ)
	90th percentile of determined occurrence time	± 0.5 year (for a signal of 6.0 cm (4σ))	± 0.1 year (for a signal of 2.0 cm (4σ))

Table 2 shows that daily-GNSS can detect all types of phenomena considered in this study to the <1 cm or <1 cm/year level accurately with less than one year of data. On the other hand, in the case of GNSS-A, a 1 cm/year-level secular crustal deformation rate can be detected by long-term observation (more than 4 years), but about 5 cm is the transient event detection limit. By increasing the observation frequency by an order of magnitude, the detection capability is significantly improved. The development of sea surface platform technology will contribute to raising future observation targets in seafloor geodetic observations. Since the detection capability changes simply in proportion to the standard

deviation of GNSS-A data, it is also necessary to improve the positioning accuracy of GNSS-A.

4.2 Slip of detectability around the Japan Trench and the Nankai Trough

Japanese government agencies have built a basic observation network for earthquakes and secular crustal deformations and are conducting regular observations to contribute disaster prevention. Japan Coast Guard has established the GNSS-A observation array, SGO-A, around the Japan Trench and the Nankai Trough to carry out regular observations in order to understand the subduction zone and the megathrust earthquake (Fig. 6). Manned vessels have been used in SGO-A, and the



present detection capability is as discussed in Sect. 4.1. It is necessary to understand the present spatial detection capability of SGO-A in order to consider future SGO-A deployment plans and in order to compare detection results with earthquake and SSE detection cases in other observation networks. Therefore, it is important to examine the scale of the phenomena that can be captured by present SGO-A ability discussed above. We verified the offshore detectability at the sea region using SGO-A compared with a case when using only the terrestrial GNSS network.

4.2.1 Method

Here, the plate boundary model is based on Japan Integrated Velocity Structure Model (Koketsu et al. 2009, 2012). The amounts of deformations on the surface are calculated using the Green's function (GF) which is calculated by the method of (Okada 1992) under the homogeneous elastic half-space condition. We divided the plate boundary into 20 km square grids and gave a slip of 20 cm to 5 m for each grid, because a subseafloor event scale to be detected is from about 20 cm (SSE, etc.) to several meters (Tohoku earthquake, etc.). Since Okada's method applies uniform slip on a given grid square, we cannot discuss spatial difference below 20 km by this numerical experiment. The dip and the strike angle of each grid follow the plate boundary model. The slip angle was fixed at 90 degrees. The GF was calculated considering the seafloor depth of each site. For seismological applications, it is convenient to express the scale of the event in terms of the moment magnitude M_w . However, M_w depends on many parameters, i.e., rigidity, amount of slip and fault size. Although some scaling laws for slip and fault size have been proposed for regular earthquakes, it is not clear for SSEs. Therefore, we evaluated the slip amount instead of the moment magnitude. Based on our test result, detection thresholds for a secular crustal deformation were set to 5 mm and 5 cm for the GEONET sites and the SGO-A sites, respectively.

4.2.2 Result

Figure 6 shows the minimum slip in each plate boundary grid that can be detected by the present observation sites. Figure 6a shows that a slip under 1.0 m cannot be detected in a broad subseafloor area (approximately half of the seafloor area considered here) in the case using only the terrestrial network. The results including the seafloor sites indicate improvement of the sensitivity; slips of about 0.2–1.0 m can be detected within a range of about 20–30 km around the seafloor sites along the Nankai Trough (Fig. 6b). Since the plate boundary is far from the seafloor on the Japan Trench side, an interplate slip of 0.2 m cannot be detected, but the detection sensitivity of

a secular crustal deformation of 1.0 m or less is improved as in the Nankai Trough. These results suggest that secular crustal deformations due to subseafloor slips of about 0.2–1.0 m or more in a range of about 100 km or more away from the land area can be detected only by SGO-A.

4.2.3 Discussion

With the present SGO-A capability, only a slip of 0.2–1.0 m or more near the seafloor site (within 20–30 km) can be detected. To detect smaller events and detail physical processes, e.g., spatiotemporal developments of SSEs and post-seismic deformations, it is necessary not only to improve the positioning accuracy and observation frequency, but also to add observation sites. An array with higher spatial coverage will allow us to analyze the location and physical process of slip events more accurately.

Brightly colored areas in Fig. 6b can also be thought of as a visualization of the present observation blank area of SGO-A. The blank areas are distributed on the west (132–134E) and east (137–138E) sides in the Nankai Trough source region and near-trench area along the Japan Trench. The present SGO-A can additionally detect a slip event of larger than 1.0 m occurred in one-third of the offshore blank area for the GEONET's detection coverage (Fig. 6a) along the Nankai Trough. However, there remains a large blank area near the Nankai Trough. These areas correspond to around the predicted source regions of future large earthquakes on the Nankai Trough side and the area with high slow earthquake activities. Also, along the Japan Trench, the blank areas correspond to around source regions of historical earthquakes. When planning the future expansion of the observation array, it is effective to consider these results and to install sites in locations where the detection capability of slip events can be improved.

5 Conclusion

We examined the event detection capability of the present GNSS-A time series data using statistical methods. We arranged the detection capability of crustal velocity, size and timing of geophysical events in Table 2. In addition to the detection capability of the present low-frequency and low-accuracy time series data by vessel-GNSS-A, we also examined the detection capability for higher observation frequency and positioning accuracy, which may be realized in the future. By constructing SGO-A, it is possible to detect slips of 1.0 m or less near the seafloor site with the step signal detection threshold of 5 cm. The result of this study quantitatively demonstrates the effectiveness of SGO-A for improving the detection capability of various geophysical phenomena due to the seismic cycle of megathrust earthquake.

Abbreviations

AIC: Akaike's information criterion; CL: Confidence level; GEONET: GNSS Earth Observation NETWORK system; GNSS: Global Navigation Satellite System; GNSS-A: GNSS-acoustic combination system; GF: Green's function; SGO-A: Seafloor geodetic observation array; SSE: Slow slip event.

Acknowledgements

We greatly thanks R. Agata and A. Nakanishi for their advice about the plate boundary model. We deeply appreciate E. Fredrickson, an anonymous reviewer and the editor for their fruitful comments. Figure 6 was prepared using the Generic Mapping Tools (Wessel et al. 2019).

Authors' contributions

TI and YY proposed the topic and constructed the accuracy verification test method. TI, YN and YY performed the accuracy verification test. SW, YN and YY performed the spatial detection test. TI and YY wrote a manuscript. All authors read and approved the final manuscript.

Funding

This study was supported by ERI JURP 2021-Y-KOBO25 in Earthquake Research Institute, the University of Tokyo.

Availability of data and materials

The dataset supporting the conclusions of this article is included within the article.

Declarations

Competing interests

The authors declare that they have no competing interest.

Author details

¹Institute of Industrial Science, University of Tokyo, 4-6-1 Komaba, Meguro-ku, Tokyo 153-8505, Japan. ²Hydrographic and Oceanographic Department, Japan Coast Guard, 3-1-1 Kasumigaseki, Chiyoda-ku, Tokyo 100-8932, Japan.

Received: 4 August 2021 Accepted: 21 October 2021

Published online: 15 November 2021

References

- Akaike H (1974) A new look at the statistical model identification. *IEEE Trans Auto Control* 19:716–723. <https://doi.org/10.1109/TAC.1974.1100705>
- Asada A, Yabuki T (2001) Centimeter-level positioning on the seafloor. *Proc Jpn Acad Ser B* 77:7–12
- Foster JH, Ericksen TL, Bingham B (2020) Wave glider-enhanced vertical seafloor geodesy. *J Atmos Ocean Tech* 37(3):417–427. <https://doi.org/10.1175/JTECH-D-19-0095.1>
- Fujita M, Ishikawa T, Mochizuki M, Sato M, Toyama S, Katayama M, Matsumoto Y, Yabuki T, Asada A, Colombo OL (2006) GPS/Acoustic seafloor geodetic observation: method of data analysis and its application. *Earth Planets Space* 58:265–275. <https://doi.org/10.1186/BF03351923>
- Iinuma T, Kido M, Ohta Y, Fukuda T, Tomita F, Ueki I (2021) GNSS-Acoustic observations of seafloor crustal deformation using a wave glider. *Front Earth Sci* 9:600946. <https://doi.org/10.3389/feart.2021.600946>
- Ishikawa T, Yokota Y, Watanabe S, Nakamura Y (2020) History of on-board equipment improvement for GNSS-A observation with focus on observation frequency. *Front Earth Sci* 8:150. <https://doi.org/10.3389/feart.2020.00150>
- Kinugasa N, Tadokoro K, Kato T, Terada Y (2020) Estimation of temporal and spatial variation of sound speed in ocean from GNSS-A measurements for observation using moored buoy. *Pro Earth Planet Sci* 7:21. <https://doi.org/10.1186/s40645-020-00331-5>
- Koketsu K, Miyake H, Afnimar TY (2009) A proposal for a standard procedure of modeling 3-D velocity structures and its application to the Tokyo metropolitan area, Japan. *Tectonophysics* 472(1–4):290–300. <https://doi.org/10.1016/j.tecto.2008.05.037>
- Koketsu K, Miyake H, Suzuki H (2012) Japan integrated velocity structure model version 1. In: *Proceedings of the 15th world conference on earthquake engineering* (1773). Lisbon
- Nakagawa H, Toyofuku T, Kotani K, Miyahara B, Iwashita C, Kawamoto S, Hatanaka Y, Mune Kane H, Ishimoto M, Yutsudo T, Ishikura N, Sugawara Y (2009) Development and validation of GEONET new analysis strategy (Version 4). *J Geograph Surv Inst* 118:1–8
- Okada Y (1992) Internal deformation due to shear and tensile faults in a half-space. *Bull Seism Soc Am* 82:1018–1040
- Sato M, Ishikawa T, Ujihara N, Yoshida S, Fujita M, Mochizuki M, Asada A (2011) Displacement above the hypocenter of the 2011 Tohoku-oki earthquake. *Science* 332:1395. <https://doi.org/10.1126/science.1207401>
- Schmalzle GM, McCaffrey R, Creager KC (2014) Central Cascadia subduction zone creep. *Geochim Geophys Geosyst* 15:1515–1532. <https://doi.org/10.1002/2013GC005172>
- Spies FN (1985) Suboceanic geodetic measurements. *IEEE Trans. Geosci. Remote Sensing* 23:502–510. <https://doi.org/10.1080/15210608509379536>
- Student (1908) The probable error of a mean. *Biometrika* 6(1):1–25. <https://doi.org/10.2307/2331554>
- Sugiura N (1978) Further analysis of the data by Akaike's information criterion and the finite corrections. *Commun Stat* 7:13–26. <https://doi.org/10.1080/03610927808827599>
- Suito H (2016) Detectability of interplate fault slip around Japan, based on GEONET daily solution F3. *J Geod Soc Jpn* 62(3):109–120. <https://doi.org/10.11366/sokuchi.62.109>
- Tadokoro K, Kinugasa N, Kato T, Terada Y, Matsuhiro K (2020) A marine-buoy-mounted system for continuous and real-time measurement of seafloor crustal deformation. *Front Earth Sci* 8:123. <https://doi.org/10.3389/feart.2020.00123>
- Watanabe S, Sato M, Fujita M, Ishikawa T, Yokota Y, Ujihara N, Asada A (2014) Evidence of viscoelastic deformation following the 2011 Tohoku-Oki earthquake revealed from seafloor geodetic observation. *Geophys Res Lett* 41:5789–5796. <https://doi.org/10.1002/2014GL061134>
- Watanabe S, Ishikawa T, Yokota Y, Nakamura Y (2020) GARPOS: Analysis software for the GNSS-A seafloor positioning with simultaneous estimation of sound speed structure. *Front Earth Sci* 8:597532. <https://doi.org/10.3389/feart.2020.597532>
- Watanabe S, Ishikawa T, Nakamura Y, Yokota Y (2021) Co- and postseismic slip behaviors extracted from decadal seafloor geodesy after the 2011 Tohoku-oki earthquake. *Earth Planets Space* 73:162. <https://doi.org/10.1186/s40623-021-01487-0>
- Wessel PL, Luis JF, Uieda L, Scharroo R, Wobbe F, Smith WHF, Tian D (2019) The generic mapping tools version 6. *Geochim Geophys Geosyst* 20:5556–5564. <https://doi.org/10.1029/2019GC008515>
- Williamson AL, Newman AV (2018) Limitations of the resolvability of finite-fault models using static land-based geodesy and open-ocean tsunami waveforms. *J Geophys Res Solid Earth* 123:9033–9048. <https://doi.org/10.1029/2018JB016091>
- Yokota Y, Ishikawa T, Watanabe S, Tashiro T, Asada A (2016) Seafloor geodetic constraints on interplate coupling of the Nankai Trough megathrust zone. *Nature* 534:374–377. <https://doi.org/10.1038/nature17632>
- Yokota Y, Ishikawa T, Watanabe S (2018) Seafloor crustal deformation data along the subduction zones around Japan obtained by GNSS-A observations. *Sci Data* 5:180182. <https://doi.org/10.1038/sdata.2018.182>
- Yokota Y, Ishikawa T, Watanabe S (2019) Gradient field of undersea sound speed structure extracted from the GNSS-A oceanography. *Mar Geophys Res* 40:493–504. <https://doi.org/10.1007/s11001-018-9362-7>
- Yokota Y, Ishikawa T (2019) Gradient field of undersea sound speed structure extracted from the GNSS-A oceanography: GNSS-A as a sensor for detecting sound speed gradient. *SN Appl Sci* 1:693. <https://doi.org/10.1007/s42452-019-0699-6>
- Yokota Y, Ishikawa T (2020) Shallow slow slip events along the Nankai Trough detected by GNSS-A. *Sci Adv* 6:eay5786. <https://doi.org/10.1126/sciadv.aay5786>
- Yokota Y, Ishikawa T, Watanabe S, Nakamura Y (2020) Kilometer-scale sound speed structure that affects GNSS-A observation: case study off the Kii channel. *Front Earth Sci* 8:331. <https://doi.org/10.3389/feart.2020.00331>
- Yoshioka S, Matsuoka Y (2013) Interplate coupling along the Nankai Trough, southwest Japan, inferred from inversion analyses of GPS data: effects of subducting plate geometry and spacing of hypothetical ocean-bottom GPS stations. *Tectonophysics* 600:165–174. <https://doi.org/10.1016/j.tecto.2013.01.023>

Publisher's Note

Springer Nature remains neutral with regard to jurisdictional claims in published maps and institutional affiliations.